2003

Comparison of Measured and Simulated Motion of a Controllable Parafoil and Payload System

Nathan Slegers
George Fox University, nslegers@georgefox.edu

Mark Costello
Georgia Institute of Technology - Main Campus

COMPARISON OF MEASURED AND SIMULATED MOTION OF A CONTROLLABLE PARAFOIL AND PAYLOAD SYSTEM

Nathan Slegers* Mark Costello†
Department of Mechanical Engineering
Oregon State University
Corvallis, Oregon 97331

ABSTRACT

For parafoil and payload aircraft, control is affected by changing the length of several rigging lines connected to the outboard side and rear of the parafoil leading to complex changes in the shape and orientation of the lifting surface. Flight mechanics of parafoil and payload aircraft most often employ a 6 or 9 DOF representation with the canopy modeled as a rigid body during flight. The effect of control inputs is idealized by the deflection of parafoil brakes on the left and right side of the parafoil. Using a small parafoil and payload aircraft, glide rates and turn performance were measured and compared against a 9 DOF simulation model. This work shows that to properly capture control response of parafoil and payload aircraft, tilt of the parafoil canopy must be accounted for along with left and right parafoil brake deflection.

NOMENCLATURE

x, y, z : Components of position vector of point C in an inertial frame.

ϕ_b, θ_b, ψ_b: Euler roll, pitch and yaw angles of payload.

ϕ_p, θ_p, ψ_p: Euler roll, pitch and yaw angles of parafoil.

$\tilde{\phi}_b, \tilde{\theta}_b, \tilde{\psi}_b$: Payload Euler roll, pitch and yaw angles for roll constraint moment computation.

$\tilde{\phi}_p, \tilde{\theta}_p, \tilde{\psi}_p$: Parafoil Euler roll, pitch and yaw angles for roll constraint moment computation.

$\dot{x}, \dot{y}, \dot{z}$: Components of velocity vector of point C in an inertial frame.

p_b, q_b, r_b: Components of angular velocity of payload in payload reference frame (b).

p_p, q_p, r_p: Components of angular velocity of parafoil in parafoil reference frame (p).

m_b, m_p : Mass of payload and parafoil.

F_{xc}, F_{yc}, F_{zc}: Components of joint constraint force in an inertial frame.

M_{xc}, M_{yc}, M_{zc}: Components of joint constraint moment in an inertial frame.

u_i, v_i, w_i : Components of relative air velocity of aerodynamic center of panel i in i^{th} frame.

V_s: Magnitude of velocity vector of mass center of payload.

u_b, v_b, w_b : Components of relative air velocity of mass center of payload in payload reference frame.

u_A, v_A, w_A : Components of relative air velocity of apparent mass center in parafoil reference frame.

x_{cb}, y_{cb}, z_{cb}: Components of vector from point C to mass center of payload in payload reference frame.

x_{cp}, y_{cp}, z_{cp}: Components of vector from point C to mass center of parafoil in parafoil reference frame.

x_{ca}, y_{ca}, z_{ca}: Components of vector from point C to apparent mass center in parafoil reference frame.

x_{pa}, y_{pa}, z_{pa}: Components of vector from parafoil mass center to apparent mass center in parafoil reference frame.

I_b, I_p: Inertia matrix of payload and parafoil.

I_F, I_M: Apparent mass force and moment coefficient matrices.

C_D^b: Drag coefficient of payload.

C_{Li}: Lift coefficient of i^{th} panel of parafoil canopy.

C_{Di}^p: Drag coefficient of i^{th} panel of parafoil canopy.

---

* Graduate Research Assistant, Department of Mechanical Engineering, Member AIAA.
† Associate Professor, Department of Mechanical Engineering, Member AIAA.

η : Angle of incidence

K_c, C_c: Rotational stiffness and damping coefficients of joint C.

A_b: Payload reference area.

A_i: Reference area of i^{th} panel of parafoil canopy.

T_p : Transformation matrix from inertial reference frame to parafoil reference frame.

T_b : Transformation matrix from inertial reference frame to payload reference frame.

T_i : Transformation matrix from i^{th} panel's reference frame to parafoil reference frame.

T_{ti} : Transformation matrix from inertial reference frame to i^{th} command trajectory reference frame.

ψ_{t_i} : Angle between inertial reference frame and i^{th} command trajectory reference frame.

F_A^b, F_A^p: Aerodynamic force on payload and parafoil in their respective frames.

M_A : Moment on parafoil due to steady aerodynamic forces.

M_{UA}: Moment on payload due to unsteady aerodynamic forces.

INTRODUCTION

New concepts for gathering real-time battlefield information rely on autonomous parafoil and payload aircraft. Relative to other air vehicles, parafoil and payload aircraft enjoy the advantage of low speed flight, long endurance, and low ground impact velocity. Control is affected by changing the length of several of the parafoil rigging lines connected to the outboard side and rear of the parafoil lifting surface. To efficiently tailor this type of aircraft to a particular design environment, dynamic modeling and simulation is applied to an idealized representation of this complex system. Flight mechanics of parafoil and payload aircraft are typically modeled using a 6 or 9 degree-of-freedom representation. In both cases, the parafoil canopy is considered a rigid body once it is inflated. There are two methods used to represent control. Perhaps the simplest method to model control forces and moments is through the use of control derivatives with the coefficients identified from flight data. The advantage of this method lies in the simplicity of the approach. The disadvantage is that little insight is provided into design parameters that effect the control response. Another method to model the control force and moment caused by the action of changes in rigging line length on each side of the parafoil is a plain flap or parafoil brake that can be deflected downward only. While more complicated, the advantage of this method lies in the close connection to design parameters of the parafoil.

Wolf and later Doherr and Schilling reported on the development of dynamic models for parachute and payload aircraft.[1,2] Hailiang and Zizeng used a 9-degree of freedom model to study the motion of a parafoil and payload system.[3] Iosilevskii established center of gravity and lift coefficient limits for a gliding parachute.[4] Brown analyzed the effects of scale and wing loading on a parafoil using a linearized model based on computer calculated aerodynamic coefficients.[5] More recent efforts by Zhu, Moreau, Accorsi, Leonard, and Smith as well as Gupta, Xu, Zhang, Accorsi, Leonard, Benney, and Stein have incorporated parafoil structural dynamics into the dynamic model of a parachute and payload system.[6,7] A significant amount of literature has been amassed in the area of experimental parafoil dynamics beginning with Ware and Hassell who investigated ram-air parachutes in a wind tunnel by varying wing area and wing chord.[8] More recently extensive flight tests have been reported on NASA's X-38 parafoil providing steady-state data and aerodynamics for large-scale parafoils.[9,10]

This paper focuses on proper modeling of the control response as a function of fundamental design parameters by modeling control response from both left and right brake deflection and canopy tilt. A comparison of flight test data and 9 degree-of-freedom simulation results for a small parafoil and payload aircraft is presented.

PARAFOIL AND PAYLOAD AIRCRAFT MODEL

Figures 1 and 2 show schematics of parafoil canopy geometry. With the exception of movable parafoil brakes, the parafoil canopy is considered to be a fixed shape once it has completely inflated. The canopy shape is modeled as a collection of panels oriented at fixed angle with respect to each other as shown in Figure 3. Deflection of the control arms on the payload causes two on the parafoil canopy. Connected to the outboard end panels are brakes that locally deflect the canopy downward. Due to the fact that the parafoil canopy is a flexible membrane, deflection of the control arms on one side of the parafoil also creates tilt of the canopy. Both these effects combine together to form the overall turning response. The parafoil canopy is connected to joint C by a rigid massless link from the mass center of the canopy. The payload is connected to joint C by a

rigid massless link from the mass center of the payload. Both the parafoil and the payload are free to rotate about joint C but are constrained by the force and moment at the joint. The combined system of the parafoil canopy and the payload are modeled with 9 degrees-of-freedom (DOF), including three inertial position components of the joint C as well as the three Euler orientation angles of the parafoil canopy and the payload. The kinematic equations for the parafoil canopy and the payload are provided in Equations 1 through 3.

$$\begin{Bmatrix} \dot{x}_c \\ \dot{y}_c \\ \dot{z}_c \end{Bmatrix} = \begin{Bmatrix} u_c \\ v_c \\ w_c \end{Bmatrix} \tag{1}$$

$$\begin{Bmatrix} \dot{\phi}_b \\ \dot{\theta}_b \\ \dot{\psi}_b \end{Bmatrix} = \begin{bmatrix} 1 & s_{\phi_b} t_{\theta_b} & c_{\phi_b} t_{\theta_b} \\ 0 & c_{\phi_b} & -s_{\phi_b} \\ 0 & s_{\phi_b} / c_{\theta_b} & c_{\phi_b} / c_{\theta_b} \end{bmatrix} \begin{Bmatrix} p_b \\ q_b \\ r_b \end{Bmatrix} \tag{2}$$

$$\begin{Bmatrix} \dot{\phi}_p \\ \dot{\theta}_p \\ \dot{\psi}_p \end{Bmatrix} = \begin{bmatrix} 1 & s_{\phi_p} t_{\theta_p} & c_{\phi_p} t_{\theta_p} \\ 0 & c_{\phi_p} & -s_{\phi_p} \\ 0 & s_{\phi_p} / c_{\theta_p} & c_{\phi_p} / c_{\theta_p} \end{bmatrix} \begin{Bmatrix} p_p \\ q_p \\ r_p \end{Bmatrix} \tag{3}$$

The dynamic equations are formed by first separating the system at the coupling joint, exposing the joint constraint force and moment acting on both bodies. The translational and rotational dynamics are inertially coupled because the position degrees of freedom of the system are the inertial position vector components of the coupling joint. The constraint force is a quantity of interest to monitor during the simulation so it is retained in the dynamic equations rather than being algebraically eliminated. Equation 4 represents the translational and rotational dynamic equations of both the parafoil and payload concatenated into matrix form.

$$\begin{bmatrix} -m_b S_c^b & 0 & m_b T_b & -T_b \\ 0 & -I_F S_c^a - m_p S_c^p & I_F T_p + m_p T_p & T_p \\ I_b & 0 & 0 & S_c^b T_b \\ 0 & I_M + I_p - S_p^a I_F S_c^a & S_p^a I_F T_p & -S_c^p T_p \end{bmatrix} \begin{Bmatrix} \dot{p}_b \\ \dot{q}_b \\ \dot{r}_b \\ \cdots \\ \dot{p}_p \\ \dot{q}_p \\ \dot{r}_p \\ \cdots \\ \ddot{x}_c \\ \ddot{y}_c \\ \ddot{z}_c \\ \cdots \\ F_{xc} \\ F_{yc} \\ F_{zc} \end{Bmatrix} = \begin{Bmatrix} \mathrm{B}_1 \\ \mathrm{B}_2 \\ \mathrm{B}_3 \\ \mathrm{B}_4 \end{Bmatrix} \tag{4}$$

The matrix in Equation 4 is a block 4 x 4 matrix where each element is a 3 x 3 matrix. Rows 1-3 in Equation 4 are forces acting on the payload mass center expressed in the payload frame and rows 7-9 are the moments about the payload mass center also in the payload frame. Rows 4-6 in Equation 4 are forces acting on the parafoil mass center expressed in the parafoil frame and rows 10-12 are the moments about the parafoil mass center also in the parafoil frame. The S_i^j matrices are cross product operator matrices, working on different vectors from i to j associated with the system configuration.

$$S_i^j = \begin{bmatrix} 0 & -z_{ij} & y_{ij} \\ z_{ij} & 0 & -x_{ij} \\ -y_{ij} & x_{ij} & 0 \end{bmatrix} \tag{5}$$

The matrix T_b represents the transformation matrix from an inertial reference frame to the payload reference frame,

$$T_b = \begin{bmatrix} c_{\theta_b} c_{\psi_b} & c_{\theta_b} s_{\psi_b} & -s_{\theta_b} \\ s_{\phi_b} s_{\theta_b} c_{\psi_b} - c_{\phi_b} s_{\psi_b} & s_{\phi_b} s_{\theta_b} s_{\psi_b} + c_{\phi_b} c_{\psi_b} & c_{\theta_b} s_{\phi_b} \\ c_{\phi_b} s_{\theta_b} c_{\psi_b} + s_{\phi_b} s_{\psi_b} & c_{\phi_b} s_{\theta_b} s_{\psi_b} - s_{\phi_b} c_{\psi_b} & c_{\phi_b} c_{\theta_b} \end{bmatrix} \tag{6}$$

while, T_p represents the transformation matrix from an inertial reference frame to the parafoil reference frame.

$$T_p = \begin{bmatrix} c_{\theta_p} c_{\psi_p} & c_{\theta_p} s_{\psi_p} & -s_{\theta_p} \\ s_{\phi_p} s_{\theta_p} c_{\psi_p} - c_{\phi_p} s_{\psi_p} & s_{\phi_p} s_{\theta_p} s_{\psi_p} + c_{\phi_p} c_{\psi_p} & c_{\theta_p} s_{\phi_p} \\ c_{\phi_p} s_{\theta_p} c_{\psi_p} + s_{\phi_p} s_{\psi_p} & c_{\phi_p} s_{\theta_p} s_{\psi_p} - s_{\phi_p} c_{\psi_p} & c_{\phi_p} c_{\theta_p} \end{bmatrix} \tag{7}$$

The common shorthand notation for trigonometric functions is employed where $\sin(\alpha) \equiv s_\alpha$, $\cos(\alpha) \equiv s_\alpha$ and $\tan(\alpha) \equiv t_\alpha$. The matrices I_b and I_p represent the mass moment of inertia matrices of the payload and the parafoil body with respect to their respective mass centers and the matrices I_F and I_M represent the apparent mass force coefficient matrix and apparent mass moment coefficient matrix respectively.

$$I_F = \begin{bmatrix} A & 0 & 0 \\ 0 & B & 0 \\ 0 & 0 & C \end{bmatrix} \tag{8}$$

$$I_M = \begin{bmatrix} I_A & 0 & 0 \\ 0 & I_B & 0 \\ 0 & 0 & I_C \end{bmatrix} \tag{9}$$

Equations 10 through 13 provide the right hand side vector of Equation 4.

$$\mathrm{B}_1 = W_b + F_A^b - m_b S_w^b S_w^b \begin{Bmatrix} x_{cb} \\ y_{cb} \\ z_{cb} \end{Bmatrix} \tag{10}$$

$$\mathrm{B}_2 = W_p + F_A^p - I_F \dot{T}_p \begin{Bmatrix} \dot{x} \\ \dot{y} \\ \dot{z} \end{Bmatrix} - S_\omega^p I_F \begin{Bmatrix} u_A \\ v_A \\ w_A \end{Bmatrix} - m_p S_w^p S_w^p \begin{Bmatrix} x_{cp} \\ y_{cp} \\ z_{cp} \end{Bmatrix} \tag{11}$$

$$\mathrm{B}_3 = M_c - S_w^b I_b \begin{Bmatrix} p_b \\ q_b \\ r_b \end{Bmatrix} \tag{12}$$

$$\begin{aligned} \mathrm{B}_4 = {} & M_A - T_p T_b^T M_c - S_w^p \left(I_p + I_M \right) \begin{Bmatrix} p_p \\ q_p \\ r_p \end{Bmatrix} \\ & - S_p^a I_F \dot{T}_p \begin{Bmatrix} \dot{x} \\ \dot{y} \\ \dot{z} \end{Bmatrix} - S_p^a S_\omega^p I_F \begin{Bmatrix} u_A \\ v_A \\ w_A \end{Bmatrix} \end{aligned} \tag{13}$$

where,

$$S_w^b = \begin{bmatrix} 0 & -r_b & q_b \\ r_b & 0 & -p_b \\ -q_b & p_b & 0 \end{bmatrix} \tag{14}$$

$$S_w^p = \begin{bmatrix} 0 & -r_p & q_p \\ r_p & 0 & -p_p \\ -q_p & p_p & 0 \end{bmatrix} \tag{15}$$

The weight force vectors on both the parafoil and payload in their respective body axes are given in Equations 16 and 17.

$$W_b = m_b g \begin{Bmatrix} -s_{\theta_b} \\ s_{\phi_b} c_{\theta_b} \\ c_{\phi_b} c_{\theta_b} \end{Bmatrix} \tag{16}$$

$$W_p = m_P g \begin{Bmatrix} -s_{\theta_p} \\ s_{\phi_p} c_{\theta_p} \\ c_{\phi_p} c_{\theta_p} \end{Bmatrix} \tag{17}$$

Equation 18 gives aerodynamic force on the payload from drag, which acts at the center of pressure of the payload assumed to be located at the payload's center.

$$F_A^b = -\frac{1}{2} \rho A_b V_b C_D^b \begin{Bmatrix} u_b \\ v_b \\ w_b \end{Bmatrix} \tag{18}$$

The payload frame components of the payload's mass center velocity that appear in Equation 18 are computed using Equation 19.

$$\begin{Bmatrix} u_b \\ v_b \\ w_b \end{Bmatrix} = T_b \begin{Bmatrix} \dot{x} \\ \dot{y} \\ \dot{z} \end{Bmatrix} + S_w^b \begin{Bmatrix} \rho_x^b \\ \rho_y^b \\ \rho_z^b \end{Bmatrix} \tag{19}$$

The shape of the parafoil canopy is modeled by joining panels of the same cross section side by side at angles with respect to a horizontal plane. The i^{th} panel of the parafoil canopy experiences lift and drag forces that are modeled using Equations 20 and 21, where u_i, v_i, w_i are the velocity components of the center of pressure of the i^{th} canopy panel in the i^{th} canopy panel frame.[11]

$$L_i = \tfrac{1}{2} \rho A_i \sqrt{u_i^2 + w_i^2}\, C_{Li} \begin{Bmatrix} w_i \\ 0 \\ -u_i \end{Bmatrix} \tag{20}$$

$$D_i = -\tfrac{1}{2} \rho A_i V_i C_{Di}^p \begin{Bmatrix} u_i \\ v_i \\ w_i \end{Bmatrix} \tag{21}$$

Equation 20 provides the total aerodynamic force on the parafoil canopy.

$$F_A = \sum_{i=1}^{n} T_i \left(L_i + D_i \right) \tag{22}$$

The applied moment about the parafoil's mass center contains contributions from the steady aerodynamic forces and the coupling joint's resistance to twisting. The moment due to a panel's steady aerodynamic forces is computed with a cross product between the distance vector from the mass center of the parafoil to the center of pressure of the panel and the force itself. Equation 23 gives the total moment from the steady aerodynamic forces.

$$M_A = \sum_{i=1}^{n} S_p^{CP_i} T_i \left(L_i + D_i \right) \tag{23}$$

where,

$$T_i = \begin{bmatrix} 1 & 0 & 0 \\ 0 & c_{\alpha_i} & -s_{\alpha_i} \\ 0 & s_{\alpha_i} & c_{\alpha_i} \end{bmatrix} \tag{24}$$

The resistance to twisting of the coupling joint is modeled as a rotational spring and damper given by Equation 25.

$$M_c = \begin{Bmatrix} 0 \\ 0 \\ K_c \left(\tilde{\psi}_p - \tilde{\psi}_b \right) + C_c \left(\dot{\tilde{\psi}}_p - \dot{\tilde{\psi}}_b \right) \end{Bmatrix} \tag{25}$$

The angles $\tilde{\psi}_p$ and $\tilde{\psi}_b$ are the modified Euler yaw angles of the parafoil and payload that come from a modified sequence of rotations where the Euler yaw angle is the final rotation. The Euler yaw angles $\tilde{\psi}_p$ and $\tilde{\psi}_b$ for the modified sequence of rotations can be related to the original Euler angles by Equations 26 and 27.

$$\tilde{\psi}_p = \tan^{-1} \left(\frac{s_{\phi_p} s_{\theta_p} c_{\psi_p} - c_{\phi_p} s_{\psi_p}}{c_{\theta_p} c_{\psi_p}} \right) \tag{26}$$

$$\tilde{\psi}_b = \tan^{-1} \left(\frac{s_{\phi_b} s_{\theta_b} c_{\psi_b} - c_{\phi_b} s_{\psi_b}}{c_{\theta_b} c_{\psi_b}} \right) \tag{27}$$

From the same modified sequence of rotations $\dot{\tilde{\psi}}_p$ and $\dot{\tilde{\psi}}_b$ are given in Equations 28 and 29.

$$\dot{\tilde{\psi}}_p = -c_{\tilde{\psi}_p} t_{\tilde{\theta}_p} p_p + s_{\tilde{\psi}_p} t_{\tilde{\theta}_p} q_p + r_p \tag{28}$$

$$\dot{\tilde{\psi}}_b = -c_{\tilde{\psi}_b} t_{\tilde{\theta}_b} p_b + s_{\tilde{\psi}_b} t_{\tilde{\theta}_b} q_b + r_b \tag{29}$$

where,

$$t_{\tilde{\theta}_p} = \frac{c_{\phi_p} s_{\theta_p} c_{\psi_p} + s_{\phi_p} s_{\psi_p}}{c_{\theta_p} c_{\psi_p}} c_{\tilde{\psi}_p} \tag{30}$$

$$t_{\tilde{\theta}_b} = \frac{c_{\phi_b} s_{\theta_b} c_{\psi_b} + s_{\phi_b} s_{\psi_b}}{c_{\theta_b} c_{\psi_b}} c_{\tilde{\psi}_b} \tag{31}$$

Given the state vector of the system, the 12 linear equations in Equation 4 are solved using LU decomposition and the equations of motion described above are numerically integrated using a fourth order Runge-Kutta algorithm to generate the trajectory of the system from it's point of release.

FLIGHT TEST AIRCRAFT DESCRIPTION

The parafoil canopy consists of 22 cells that are formed by airfoil-shaped fabric ribs, has a surface area of 13.1 ft^2 and an aspect ratio of 3.6. The canopy is connected to the payload through two sets of suspension lines with each set consisting of four spanwise rows and three chordwise columns. Each grid of suspension lines is collected into a single suspension line that is then connected to the payload. Four control lines, two on each side, control the parafoil. The control lines on each side originate from half the chord length on the outboard edge of the canopy and 16" form the outboard edge on the rear of the canopy and are collected into a single control line for the side as shown in Figures 1 and 2.

The payload consists of an aluminum frame, three control servos, a 0.40 series glow engine and 10 x 6 pusher propeller, and an electronic control unit (ECU). Control of the system is accomplished through three servos, one for the engine throttle and two for the canopy control lines. The engine and propeller allow flight testing to be repeated easily and inexpensively by enabling the parafoil and payload aircraft to be launched from ground level and flown to appropriate altitudes where the engine is stopped and non-powered flight is commenced. The payload is shown in Figure 4 and the complete system is shown during flight in Figure 5. The ECU completes three tasks, recording control inputs, receiving Global

Positioning Satellite (GPS) information, and wireless transmission to a computer on the ground. The internal electronics of the ECU contain the radio receiver for the control servos, Motorola Oncore GPS receiver, MaxStream wireless transceiver, batteries, and supporting electronics.

FLIGHT TEST DESCRIPTION

A total of five flight tests were completed. Flights tests 1, 3, and 5 were given equal control deflections of increasing magnitude on both sides. Flights 2 and 4 had no control deflection on the left side of the canopy and the same deflection as 3 and 5 respectively on the right side. The control scheduling for the flights are summarized in Table 1. Flights 1, 3, and 5 were to maintain cross range to a minimum with the parafoil and payload aircraft gliding down range to establish the glide rate. Aerodynamic coefficients of the parafoil and payload aircraft are then estimated. Flights 2 and 4 create a steady turn by constant deflection of the right control line with equal magnitudes to flights 3 and 5.

Flight tests were initiated by powering the ECU and allowing a 3-D satellite fix to be achieved by the GPS receiver, usually occurring in less than 180 sec. Once a 3-D fix was achieved the glow engine was started and the parafoil and payload aircraft was hand launched. The parafoil and payload aircraft was powered to climb to an altitude of at least 350 ft above the ground. At sufficient altitude, control was used to minimize any turn rates of the aircraft and the engine was stopped. Control inputs for the flight tests were immediately commanded at the onset of non-powered flight. During non-powered portions of flights 1, 3, and 5 small control inputs were used to minimize cross range without disturbing glide rates. Complete results from flight 1 are shown in Figures 6 through 8 with a square designating the point where a steady state glide begins and a circle where control inputs are used initiate a flare maneuver. In Figure 6 the first 30 seconds of data are used to acquire a 3-D fix with the GPS receiver. Launching of the system occurs at a time of 30 sec and from a time of 30 to 120 sec altitude data is erratic due to maneuvering during initial climb. After 120 sec the aircraft trims to a steady climb and less dramatic turn rates occur. Engine power is stopped at a time of 165 sec when a ground altitude of 375 ft is achieved. The non-powered portion of flight 1 lasts 51 sec at which time the control lines are used to create a soft landing. Figure 7 shows the 2-D position of the parafoil system during the flight. Figure 8 shows the control deflections used during the flight.

The same procedure from flight 1 was followed for flight 2, however once the engine was stopped only the right control line was deflected and a steady turn results. Figure 9 shows the full 2-D path of flight 2 with the solid line representing the time of constant right brake deflection and a square representing the start of non-powered flight. A circle indicates the beginning of a flare maneuver. Flight 2 control deflections are shown in Figure 10. The procedure from flight 1 was repeated for flights 3 and 5 while increasing control deflections. Flight 4 followed a similar procedure to flight 2.

RESULTS

Flights 1, 3, and 5 are used to estimate the glide rates for the three control cases: (L 0" / R 0"), (L 1.375"/R 1.375") and (L 2.875"/R 2.875"). Glide rates are estimated by first removing the section of non-powered flight after steady glide rate has begun but before the final flare maneuver is started, which is shown for flight 1 as the solid line in Figure 6. Next, the 2-D positions are converted to total distance traveled because as seen in Figure 6 the parafoil does not travel a straight line due to small disturbances and non-zero yaw and roll rates at the onset of non-powered flight. Finally, the total distance traveled is plotted vs. altitude. Figure 11 shows the glide rates for flights 1, 3, and 5 where the altitude at initial steady glide rate for all three cases was started at zero for comparison. Glide rates are estimated to be –0.32, –0.29 and –0.23 by a linear least squares fit to the flight data.

The estimated glide rates can be used to estimate the lift and drag coefficients needed in the dynamic model. Considering flight 1 the estimated glide rate of –0.32 can be supplemented by the average velocity of the non-powered flight estimated to be 22.4 ft/s by using the total distance traveled of 1073 ft and the flight time of 48 sec. Parafoil lift and drag coefficients are a linear function of angle of attack with the zero angle of attack coefficients being about two-thirds the trimmed aerodynamic coefficients. The dynamic model using the physical parameters listed in Table 2 and the six apparent mass coefficients based on formulas by Lissaman and Brown[14] listed in Table 3 are used to estimate the aerodynamic coefficients. The estimated aerodynamic coefficients are listed in Table 4.

Using the estimated aerodynamic coefficients the dynamic model is used to compare the turn rates from the simulations of flight 2 (L 0"/R 1.375") and flight 4 (L 0"/R 2.875"). Figures 12 and 13 show the cross range and turn rates from the simulation of flight 2. With only the effect of parafoil brake deflection in the model, response to

right control deflection is a sharp spiraling turn with negative turn rates, in contrast to the smooth positive turn rate measured from the experimental system. This response is caused by the large predicted increase in lift from control deflection required for the glide rates in flights 3 and 5. Now that only one side has a control deflection the increased lift causes a banking of the canopy to the opposite direction. Modeling the deflection of one control line more than the other simply by a rear panel deflection does not adequately capture the dynamics for this experimental system. The control line on each side is attached to both a rear flap and the edge of the canopy as shown in Figure 1. Deflection of the control on one side more than the other side not only deflects the rear flaps but also creates subtle tilting of the canopy to one side. This suggests that the model should also adjust the panel angles during control inputs. The exact amount of canopy tilting falls between two extreme cases of zero and full canopy tilt. Figure 14 presents the geometry for the control arms and the range of canopy tilt for flight 1 is between 0 and 5.5 deg and between 0 and 10.4 deg for flight 2, with the actual canopy tilt falling between the two extremes. Using the 9 DOF model it was found that 1.375 deg of canopy tilt was required to replicate the turn rates from flight 2 and 2.970 deg for flight 4. Figures 15 and 16 show measured and simulated turn rates for flights 2 and 4 with canopy tilt added to the simulation model.

Due to fact that parafoil canopies are flexible membranes, pulling down on the canopy on one side causes the parafoil brake to deflect and also causes the parafoil canopy to tilt down on the side where the brakes are deflected. This phenomenon is true not only for configurations where one or more of the control lines is connected to the side of the parafoil but also configurations where the control lines are connected to the outboard rear of the canopy only. It is also interesting to note that the effects of parafoil brake deflection and canopy tilt cause response in different directions. For low glide rate parafoils where the lift to drag ratio is large, parafoil brake deflection causes a roll steer effect where brake deflection creates increased lift leading to roll and yaw. Thus the effect of pure right parafoil brake deflection may causes a left turn when the parafoil lift to drag ratio is large. On the other hand when the canopy tilts to the right the lift force also tilts to the right leading to a right turn. The actual control response is a complex phenomenon where two opposing effects are combined for overall control response.

CONCLUSIONS

Dynamic simulation models for flight mechanics of parafoil and payload aircraft most often employ a 6 or 9 DOF representation. During flight, the parafoil canopy is modeled as a rigid body. The affect of control inputs is idealized by deflection of parafoil brakes on the left and right side of the parafoil. Using a small parafoil and payload aircraft, glide rate and turn performance was measured and compared against a 9 DOF simulation model. The experimental aircraft control line connection to the parafoil consisted of two lines on the outboard rear section of the parafoil and two lines on the outboard side of the parafoil causing both effective brake deflection along with canopy tilt. When contrasting the flight test data with simulation results, it was found that using only parafoil brake deflection in the model could not replicate the turn response of the aircraft. In fact, with only parafoil brake deflection in the model, steering in the opposite direction of the experimental data is exhibited. However, when both parafoil brake deflection and canopy tilt is included in the simulation model, turn performance of the system can be well replicated. Thus, for controllable parafoil and payload aircraft a dynamic model should include the effect of right and left parafoil brake deflection and canopy tilt to replicate system turning dynamics.

REFERENCES

1. Wolf, D., "Dynamic Stability of Nonrigid Parachute and Payload System," *Journal of Aircraft*, Vol. 8 No. 8, pp. 603-609, 1971.
2. Doherr, K., Schiling, H., "9 DOF-simulation of Rotating Parachute Systems," AIAA 12th. Aerodynamic Decelerator and Balloon Tech. Conf, 1991.
3. Hailiang, M., Zizeng, Q., "9-DOF Simulation of Controllable Parafoil System for Gliding and Stability," *Journal of National University of Defense Technology*, Vol. 16 No. 2, pp. 49-54, 1994.
4. Iosilevskii, G., "Center of Gravity and Minimal Lift Coefficient Limits of a Gliding Parachute," *Journal of Aircraft*, Vol. 32 No. 6, pp. 1297-1302, 1995.
5. Brown, G.J, "Parafoil Steady Turn Response to Control Input," AIAA Paper 93-1241.
6. Zhu, Y., Moreau, M., Accorsi, M., Leonard J.,Smith J., "Computer Simulation of Parafoil Dynamics," AIAA 2001-2005, AIAA 16th Aerodynamic Decelerator

Systems Technology Conference, May 2001.
7. Gupta, M., Xu, Z., Zhang, W., Accorsi, M., Leonard, J., Benney R., Stein., "Recent Advances in Structural Modeling of Parachute Dynamics," AIAA 2001-2030, AIAA 16th Aerodynamic Decelerator Systems Technology Conference, May 2001.
8. Ware, G.M., Hassell, Jr., J.L., "Wind-Tunnel Investigation of Ram-Air_Inflated All-Flexible Wings of Aspect Ratios 1.0 to 3.0," NASA TM SX-1923,1969.
9. Iacomini, C.S., Cerimele, C.J., "Lateral-Directional Aerodynamics from a Large Scale Parafoil Test Program," AIAA Paper 99-1731.
10. Iacomini, C.S., Cerimele, C.J., "Longitudinal Aerodynamics from a Large Scale Parafoil Test Program," AIAA Paper 99-1732.
11. Lissaman, P.B.S., Brown, G. J., "Apparent Mass Effects on Parafoil Dynamics," AIAA Paper 93-1236

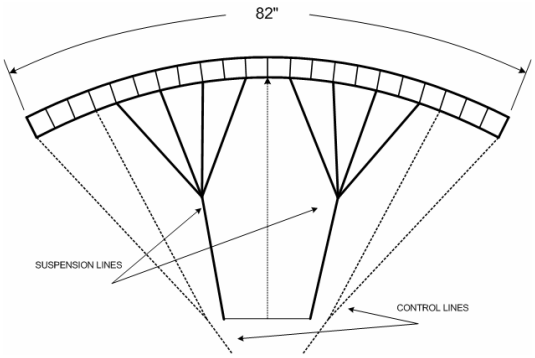

Figure 1- Front View of Parafoil Canopy

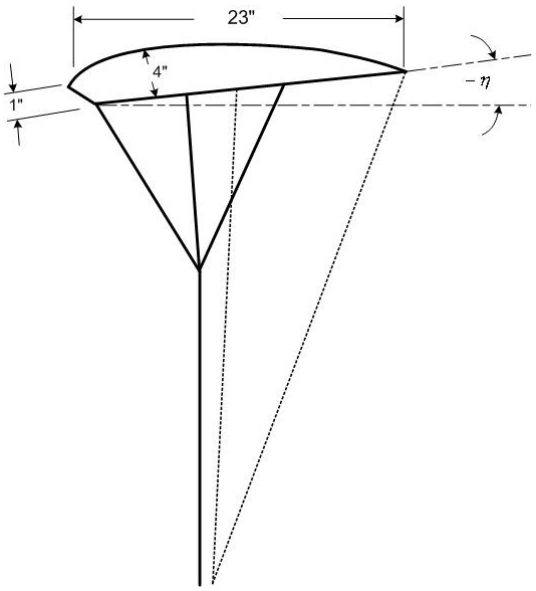

Figure 2- Side View of Parafoil Canopy

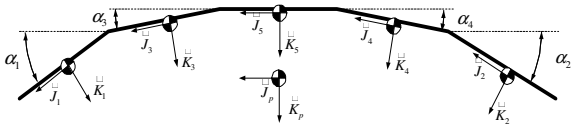

Figure 3 – Parafoil Canopy Geometr

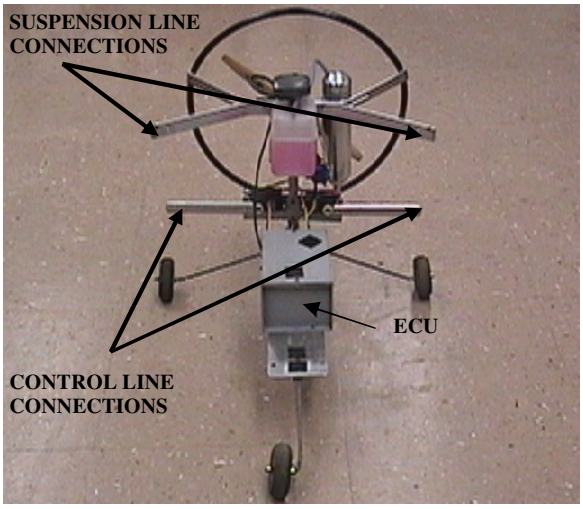

Figure 4 – Payload

Figure 5 – Parafoil and Payload in Flight

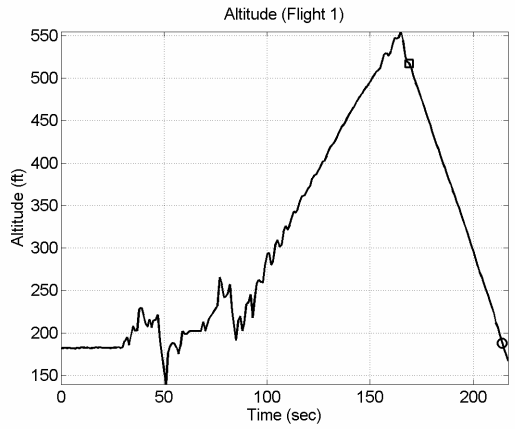

Figure 6 – Flight 1 (L 0”/R 0”) Altitude

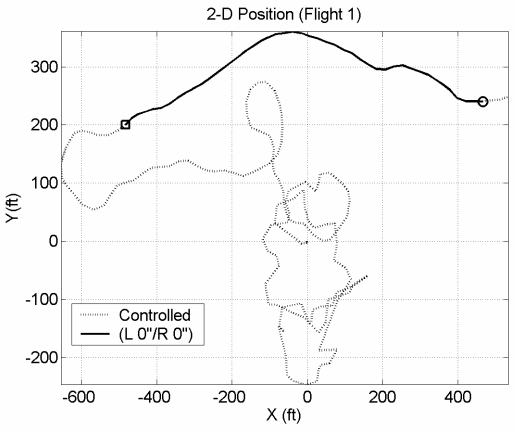

Figure 7 – Flight 1 (L 0”/R 0”) 2-D Position

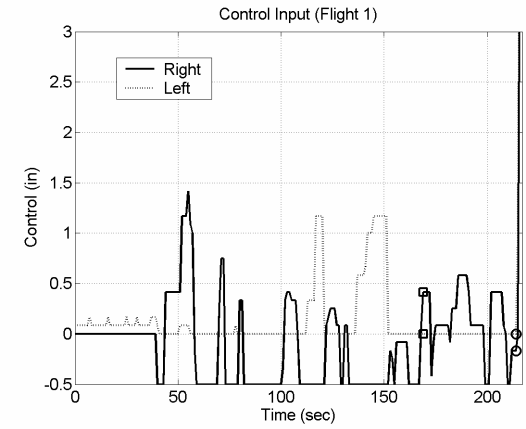

Figure 8 – Flight 1 (L 0”/R 0”) Control Deflections

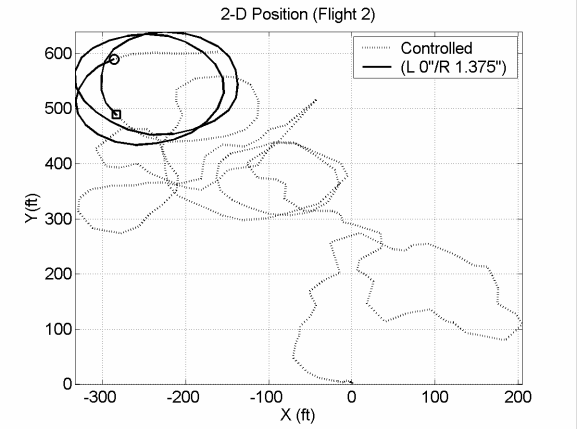

Figure 9 – Flight 2 (L 0”/R 1.375”) 2-D Position

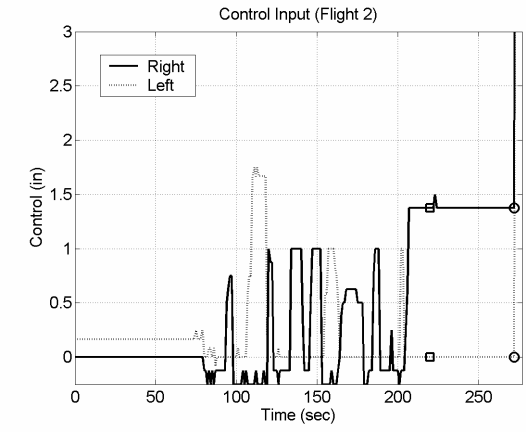

Figure 10 – Flight 2 (L 0”/R 1.375”) Control Deflection

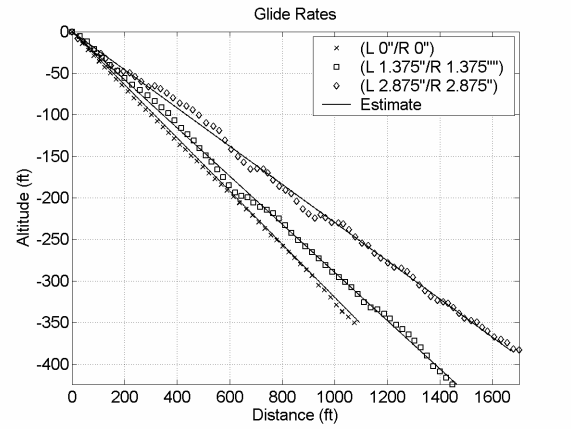

Figure 11 – Estimated Glide Rates

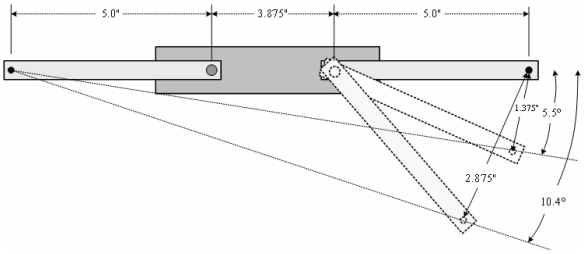

Figure 14 – Servo Geometry

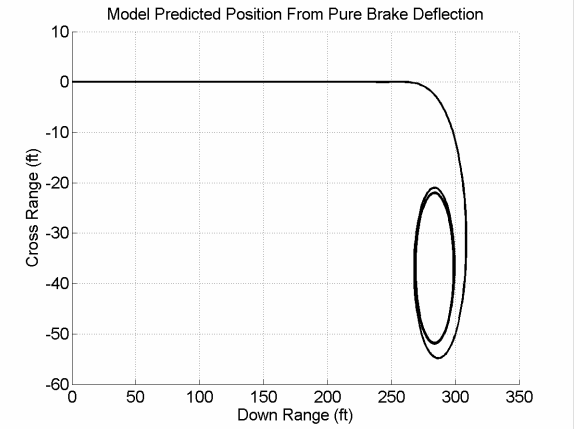

Figure 12 – Model Prediction of Flight 2 (L 0"/R 1.375") Cross Range

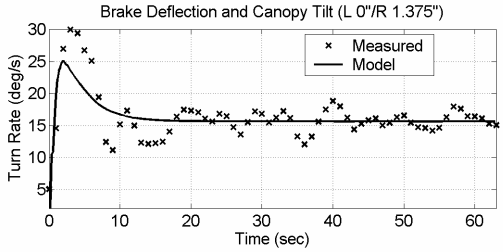

Figure 15 – Canopy Tilt Corrected Model Prediction of Flight 2 (L 0"/R 1.375") Turn Rate

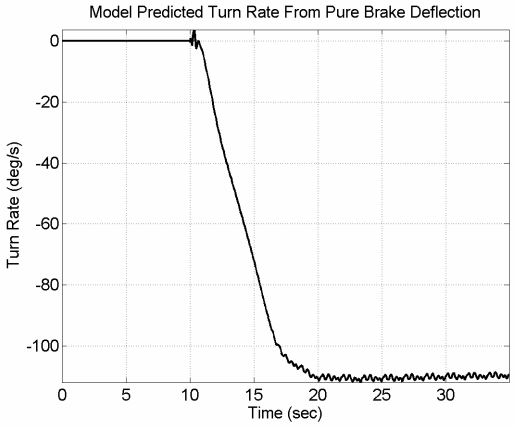

Figure 13 – Model Prediction of Flight 2 (L 0"/R 1.375") Turn Rate

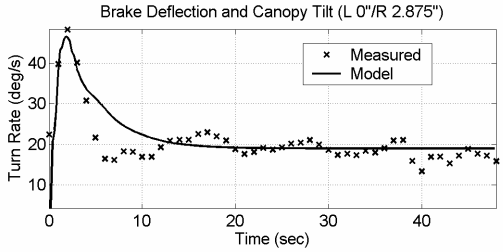

Figure 16 – Canopy Tilt Corrected Model Prediction of Flight 2 (L 0"/R 2.875") Turn Rate

Table 1 – Flight Testing Control Deflections

Flight Test Number	Control Deflection
1	(L 0”/R 0”)
2	(L 0”/R 1.375”)
3	(L 1.375”/R 1.375”)
4	(L 0”/R 2.875”)
5	(L 2.875”/R 2.875”)

Table 2 – Physical Parameters

Parameter	Value	Description
n	5	Number of Panels
α_1	25 deg	Panel 1 Angle
α_2	-25 deg	Panel 2 Angle
α_3	20 deg	Panel 3 Angle
α_4	-20 deg	Panel 4 Angle
α_5	0 deg	Panel 5 Angle
η	-11.5 deg	Incidence Angle
S	2.61 ft^2	Panel Area
t	4 in	Panel thickness
w_p	0.45 lbf	Parafoil Weight
w_s	4.1 lbf	Payload Weight

Table 3 – Apparent Mass Coefficients

Coefficient	Value
A	0.0019
B	0.00021
C	0.044
I_A	0.11
I_B	0.010
I_C	0.0070

Table 4 – Estimated Aerodynamic Coefficients

Parameter	Flight 1	Flight 3	Flight 5
α (deg)	7.4	5.7	2.8
$C_L(\alpha_T)$	.571	.757	1.08
$C_D(\alpha_T)$	.168	.169	.161